Proof of concept validation of bioresorbable optical fibers for diffuse correlation spectroscopy

Research Article Vol. 15, No. 11 / 1 Nov 2024 / Biomedical Optics Express 6384
Biomedical Optics EXPRESS

Proof of concept validation of bioresorbable optical fibers for diffuse correlation spectroscopy

JAWAD T. PANDAYIL,[1,2] NADIA G. BOETTI,[1] DAVIDE JANNER,[2] TURGUT DURDURAN,[3,4] AND LORENZO CORTESE[4,*]

[1]Fondazione LINKS-Leading Innovation and Knowledge for Society, via P. C. Boggio 61, 10138 Torino, Italy
[2]Dipartimento di Scienza Applicata e Tecnologia (DISAT) and RU INSTM, Politecnico di Torino, Corso Duca degli Abruzzi 24, 10129 Torino, Italy
[3]Institució Catalana de Recerca i Estudis Avançats (ICREA), E-08010 Barcelona, Spain
[4]ICFO-Institut de Ciències Fotòniques, The Barcelona Institute of Science and Technology, Av. Carl Friedrich Gauss, 3, 08660 Castelldefels (Barcelona), Spain
*lorenzo.cortese@icfo.eu

Abstract: Optical quality bioresorbable materials have been gaining interest in recent years for various interstitial biomedical/medical application. An example of this is when the implant gradually dissolves in the body, providing physiological information over extended periods of time, hence reducing the need for revision surgeries. This study reports for the first time the in-house fabrication of single mode (at 785 nm) calcium phosphate glass (CPG) based bioresorbable optical fibers and investigates their suitability for microvascular blood flow monitoring using diffuse correlation spectroscopy (DCS). *Ex vivo* experiments in liquid phantom and non-invasive *in vivo* experiments on the human forearm muscle were conducted using multimode and single mode CPG bioresorbable optical fibers. The retrieved flow index from the correlation curves acquired using CPG fibers was in good agreement with that obtained using standard silica (Si) fibers, both *ex vivo* and *in vivo*. The results demonstrate the potential of CPG optical fibers for further exploration.

1. Introduction

Optical quality bioresorbable materials are widely being explored for the design and development of implantable devices to meet various clinical needs involving interstitial light delivery and detection [1]. Recent studies demonstrate implantable and resorbable photonic crystal structures and Fabry-Perot interferometer designs for continuous and precise measurement of intracranial pressure and temperature [2], implantable optical probes to monitor neural activity, cerebral temperature and oxygenation [3], and, optical wave guides for biochemical sensing [4]. Such implants dissolve in the physiological environment over a controlled and clinically relevant timescale, bypassing the need for surgical extraction, hence reducing the costs and the risks, distress and pain to the patient [5]. The extended information on internal physiological parameters acquired from these types of implants could inform about the local tissue health, pharmacological drug-delivery schedules, surgical intervention procedures and the management of recovery and rehabilitation [3].

A promising class of optical implants consists of implantable optical fibers, which can deliver light deep into a localized area and collect the light that is reflected, scattered, or fluorescently emitted from a tissue specimen, hence finding a wide range of potential biomedical applications, including monitoring of different biomarkers important for diagnostic and treatment applications [6]. Among various types of optical fibers that have been reported for different biomedical applications [7], we focus on calcium phosphate glass (CPG) based optical fibers. CPG based

#540137 https://doi.org/10.1364/BOE.540137
Journal © 2024 Received 22 Aug 2024; revised 6 Oct 2024; accepted 6 Oct 2024; published 16 Oct 2024

Biomedical Optics EXPRESS

materials are well-known for their bioresorbable property and have been widely investigated over the past fifty years for various biomedical applications [8,9]. By suitably tailoring the composition of the glass system, an optical quality (wide window of transparency from UV to NIR region) CPG composition suitable for fiber drawing was developed in 2016 [10]. These fibers dissolved *in vitro* in Phosphate Buffer Saline (PBS) solution and no clinical signs of adverse effect was observed during the *in vivo* subcutaneous implantation of these fibers in rats [11]. Here, we focus on the applications of CPG optical fibers in diffuse optical technologies for monitoring tissue hemodynamics and metabolism.

CPG based multimode (MM) optical fibers have been recently validated for near-infrared time domain diffuse optical spectroscopy (TD-DOS), a diffuse optical technique allowing continuous monitoring of local tissue oxygenation (StO2), blood volume (i.e. total hemoglobin concentration, THC), tissue composition and structure [12,13], paving the way for interstitial continuous monitoring of tissue oxygenation.

TD-DOS is often associated with a different near-infrared diffuse optical modality, diffuse correlation spectroscopy (DCS), to provide diversified and complementary information about tissue hemodynamics and metabolism [14]. Differently from TD-DOS, which studies the delay and distortion of short laser pulses due to the interaction with the tissue, DCS uses long coherence continuous wave laser light and, by using single mode (SM) optical fibers, detects laser speckle fluctuations induced by light scattering by moving red blood cells to quantify microvascular blood flow in the deep tissue (>1 cm). Blood flow measurements with DCS have been well validated and tested in numerous clinical scenarios [14–22]. Of particular relevance, DCS has also been employed for interstitial applications, to monitor blood flow response during interstitial human prostate photo dynamic therapy (PDT) [23,24], and to detect spinal cord ischemia during surgery [25].

As an intermediate step towards the clinical use of implantable and resorbable optical fibers for interstitial monitoring, in the present study, we conducted ex *vivo* and non-invasive *in vivo* DCS measurements using in-house fabricated CPG fibers. Here, we have reported for the first time, the in-house realization of SM CPG bioresorbable optical fibers at 785 nm for light collection in DCS. These SM fibers, along with MM CPG fibers for light delivery, were evaluated for their precision in retrieving the scatterer's Brownian diffusion coefficient (Db) in liquid phantom, where MM standard silica fibers and custom fabricated CPG fibers were alternatively used to deliver the light, and SM silica and CPG fibers to simultaneously collect the diffused light. These fibers were then also tested for their potential in *in vivo* non-invasive conditions, by monitoring dynamic changes in blood flow index (BFI) during a vascular occlusion test (VOT) performed on human forearm muscle. Lastly, high temporal resolution DCS *in vivo* acquisition on the human forearm muscle were performed simultaneously using SM CPG and silica fibers, and the data collected were analyzed and compared for their capability in detecting pulsatile blood flow signal.

2. Materials and methods

2.1. Optical fiber fabrication, characterization, and connectorization

Two types of bioresorbable CPG optical fibers, one MM and one SM were fabricated for this study. Initially, two pairs of core and cladding glasses (one for SM and the other for MM fiber) were synthesized through conventional melt-quenching method using high purity biocompatible chemicals (P_2O_5-CaO-Na_2O-SiO_2-MgO). The molar concentrations of CaO and MgO in the glass composition were selected based on the previous study reported in [10], which demonstrated a linear decrease in refractive index values with increasing MgO molar content as a substitute of CaO. During glass synthesis, the goal was to achieve a refractive index difference between the core and cladding glasses that would result in a numerical aperture *NA* comparable to that of standard fibers employed in DCS applications (see section 3.1). The wavelength-dependent refractive index $n(\lambda)$ of the core and cladding glasses were measured at different wavelengths

Biomedical Optics EXPRESS

(633, 855, 1061, 1312, 1533 nm) through a Metricon 2010 prism coupler (Metricon corporation, US) with an estimated error of ±0.0005. Refractive index at 785 nm (i.e. the wavelength used for DCS experiments, see section 2.2) was then obtained through interpolation using Cauchy's equation [26]. The numerical aperture *NA* of the SM and MM fibers was calculated as $NA=\sqrt{(n_{core}{}^2 - n_{cladd}{}^2)}$, where n_{core} is the refractive index of core glass and n_{cladd} is the refractive index of the cladding [27].

The cores (rods) were then obtained by casting the melt into a cylindrical mold to form 12 mm diameter rods, while the claddings (tubes) were obtained through glass extrusion. The MM core rod was then stretched into a 5 mm diameter rod and the SM core rod to a 0.4 mm rod to fit them exactly into the holes of the extruded MM and SM cladding tubes. The rods were inserted into their respective tubes to form rod-in-tube preforms. One-meter sections of MM optical fiber were obtained by stretching the preform (drawing temperature: 671 °C, drawing speed: 55 cm/minute) while several meters of the SM fiber were collected on a winding drum (Drawing temperature: 665 °C, drawing speed: 3 m/minute and tension: 27 g) during the drawing process. Both operations were performed using a drawing tower developed in-house. The details about these fabrication methods can be found in previous publications [10,28,29].

Optical microscopy using Nikon ECLIPSE E 50i (Nikon Instruments Inc, US) (equipped with image analysis software ToupView) was performed on different sections of the fiber during the drawing process to assess their dimensions and overall quality. Particular attention was given to the assessment of the core/cladding interface quality, core alignment and the homogeneity in the micrograph as these parameters can heavily influence optical loss. The attenuation loss of the fabricated fibers were measured by cut-back method [30] on fiber samples of different lengths at 660 nm. The *V*-number of the SM fiber was calculated using the theoretical formula $(V = \frac{2\pi}{\lambda} \times (r_{core}) \times NA$, where λ is the wavelength and r_{core} is the radius of the core [27].

The MM fiber was FC-PC connectorized at one end, to directly connect it to the DCS laser unit. For the connectorization, the protocol explained in [31] was followed. The other end of the fiber, that extends towards the sample, was cleaved (cleaver CT-106, Fujikura, Japan) to have a clean and flat fiber cross-section. After the cleaving and connectorization processes, the MM fiber length was 90 cm. From the long original SM fiber collected on the winding drum, two sections of 15 cm were cut and cleaved. These short sections of SM fiber were chosen to compensate for their higher optical loss over the length of the fiber, which will be later detailed in section 3.1. The first section was FC-PC connectorized at one end as explained previously for MM fiber. For the DCS measurement convenience, this FC-PC connectorized section was then connected to a one-meter FC-PC silica patch cord (780 HP, Thorlabs, US) using FC-PC mating sleeve (this is referred to as configuration-1 in the following sections of the paper, see section 2.3), for being connected to the DCS detection system. Due to the very small core size (< 5 µm diameter) of the SM fiber, any slight misalignment between the cores of the CPG SM and patch cord can be possible due to the manual connectorization, creating additional optical loss. To ensure a better core alignment and thus the reduced optical loss, the second 15 cm section obtained from the original CPG SM fiber was spliced to a commercial one-meter SM fiber pigtail (780 HP, Thorlabs, US) using a CO_2 laser splicer (LZM-100, Fujikura, Japan), where the automated core alignment between the fibers is possible (fiber configuration-2, see section 2.3). Details of these two fiber configurations used in the measurements are depicted in Fig. 1(a).

2.2. DCS set-up

A custom built DCS device was used for the experiments combining emission at 785 nm from a single longitudinal mode continuous wave laser (iBEAM SMART 785, Toptica, Germany) with four detectors (SPCM-AQ4C, Excelitas, Canada) and a four-channel hardware multi-tau correlator (custom product, HemoPhotonics S. L., Castelldefels, ES) for real time calculation of the intensity temporal autocorrelation function g_2 [32]. In the experiments reported here,

Biomedical Optics EXPRESS

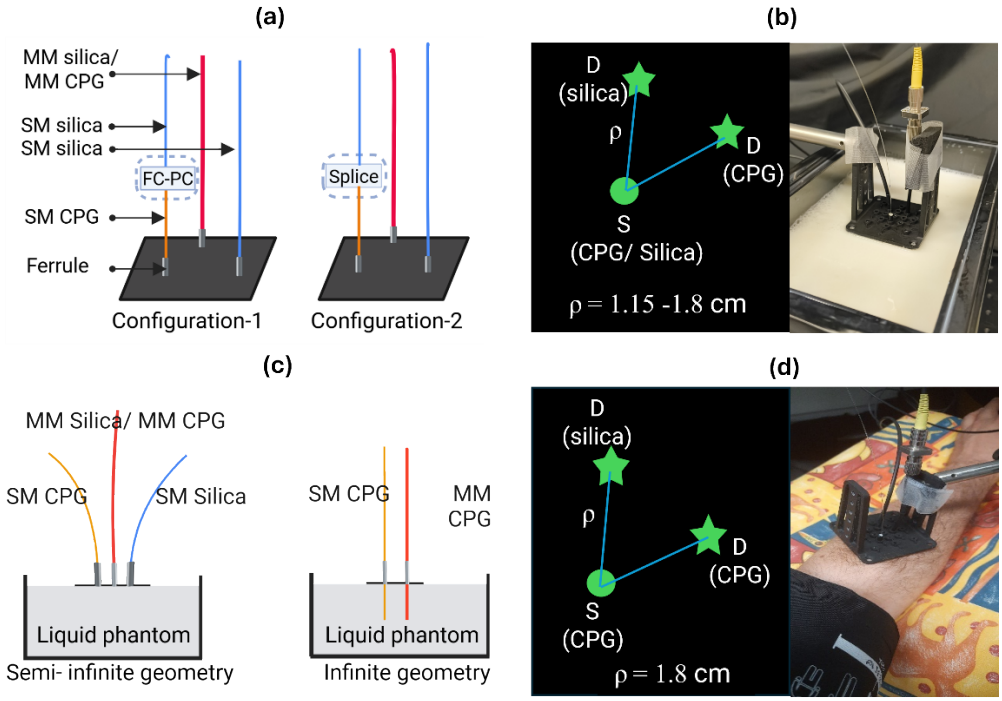

Fig. 1. (a) Schematic representation of the two fiber configurations used on the detection side (as detailed in Table 1) and of the custom fiber holder. In configuration 1, FC-PC connectorized SM CPG fiber is connected to the FC-PC 780 HP SM commercial patch cord using an FC-PC mating sleeve. In configuration 2, SM CPG fiber and a 780 HP SM commercial fiber are connected through a hybrid splice using a CO_2 laser splicer. (b) Schematic representing the positioning of fiber's tips over the custom-made fiber holder for the *ex vivo* experiments ('S' represents the source fiber and 'D' represents the detection fiber where source fiber position is represented in circle and detection fiber's position using stars). (c) Schematic of the *ex vivo* measurement set-up in semi-infinite medium geometry, where the fiber tips are placed at the liquid phantom surface, and in infinite medium geometry where the fibers are immersed in the liquid phantom. (d) Fiber arrangement and the experimental set-up during the *in vivo* vascular occlusion test.

only two detection channels were used. The laser light was injected through a MM fiber of 200 µm core and the diffuse reflectance collected through SM fibers at 785 nm. As anticipated in the previous sections and reported in detail in the following sections, for *ex vivo* and *in vivo* experiments we used alternatively as source fiber a commercial three-meter silica MM fiber (FT200 EMT, Thorlabs, US) and an in-house manufactured MM CPG fiber (see section 3.1), and, as detection fibers, a commercial three-meter SM fiber (780 HP, Thorlabs, US) and an in-house manufactured SM CPG fiber.

2.3. *Ex vivo measurement*

Ex vivo measurements were performed on a liquid phantom which consists of an emulsion of lipid droplets (Lipofundin 20%, B. Braun Melsungen AG, Germany) in purified water. The concentration of Lipofundin 20% in water was chosen to obtain a reduced scattering coefficient (μ_s') of 5 cm^{-1} and water absorption at 785 nm as described in [33].

The liquid phantom was placed in a black plastic phantom box (25 cm(l), 15 cm(b), 18 cm(h)) with the top side open to allow access of the custom-made fiber holder, as represented in the

Biomedical Optics EXPRESS

schematics of Fig. 1(c). The phantom study consisted of nine independent measurements, as reported in Table 1, where eight of them in semi-infinite medium geometry, with fiber tips laying on the liquid surface, and one in infinite medium geometry, with fibers immersed eight centimeters into the liquid, as reported in Fig. 1(c). For the semi-infinite medium geometry measurements (points 1 to 8 of Table 1), signals were simultaneously acquired from two detection fibers (one CPG and one silica) placed in the reflectance geometry. The detection fiber tips were positioned symmetrically with respect to the silica and CPG source fibers, as shown in the schematic in Fig. 1(b). During each measurement, light was emitted from a single source fiber, i.e., silica MM and CPG MM alternatively. During the experiments, MM and SM CPG bare fiber tips were placed inside standard ceramic ferrules (with bore sizes 440 µm and 270 µm respectively) which were fixed to the probe (Fig. 1(a)). Measurements were repeated at two different source-detector distances (ρ = 1.8 cm and 1.15 cm) in both detection fiber configurations-1 and 2.

Table 1. Details of the ex vivo measurements performed on the liquid phantom.

	ρ (cm)	Source (S)	Detector (D)
1	1.8 cm	Silica	Configuration-1 (Semi-infinite geometry)
2		CPG	
3	1.15 cm	Silica	
4		CPG	
5	1.8 cm	Silica	Configuration-2 (Semi-infinite geometry)
6		CPG	
7	1.15 cm	Silica	
8		CPG	
9	1.5 cm	CPG	Configuration-2 (Infinite geometry)

In the case when the fibers are immersed in the liquid phantom (infinite medium geometry, measurement 9 in Table 1) to simulate the interstitial acquisition, only one measurement was performed with a single pair of source and detector fibers, where the light is injected through a MM CPG fiber and collected through a SM CPG fiber in configuration-2, at a ρ = 1.5 cm (see Fig. 1(c)).

Each experiment consisted of the acquisition of 120 g_2 curves with one second average time each (total measurement duration of two minutes). The intensity of the injected light was attenuated using a manual optical attenuator which is part of the DCS system to obtain the detected photon count rate < 400 kHz in all the measurements, in accordance with detector and autocorrelator specifications. A dark count < 0.5 kHz was ensured before each measurement, by covering the set-up with a black, light-proof curtain.

2.4. *In vivo measurement*

To test the capability of CPG fibers in tracking changes in blood flow, we have performed a vascular occlusion test (VOT) by monitoring the blood flow in the forearm muscle (*brachioradialis* muscle) during a short period of induced ischemia [32,34] on one healthy human subject. The measurements were conducted according to the guidelines of the Declaration of Helsinki and approved by the local Ethic Committee (ref. ICFO_HCP/2012/1). The subject was asked to sign the informed consent form.

The VOT test protocol consisted of three phases, which include the acquisition of an initial baseline signal for three minutes, an arterial occlusion phase, i.e. ischemia, induced by inflating a typical arm blood-pressure cuff placed on the biceps at a cuff pressure of 180 mmHg for three minutes, and a final recovery phase of five minutes after rapidly releasing the cuff pressure. The

Biomedical Optics EXPRESS

laser power injected into the tissue was limited to 27 mW to respect the maximum permissible exposure in accordance with the International Organization for Standardization (ISO) and the American National Standards Institute (ANSI). The photon count rate and g_2 curves were recorded with an integration time of one second. The CPG source fiber and the pair of detection fiber (silica and FC-PC connectorized CPG, that is, configuration-1) were placed symmetrically 1.8 cm apart as reported in Fig. 1(d).

Lastly, we performed a five-minute measurement on the same subject forearm muscle at rest, with an acquisition rate of 38 Hz (integration time of 26 ms), to test the possibility of capturing the hemodynamics of the entire cardiac cycle by detecting the pulsatile blood flow [35]. The fiber configuration was the same as the VOT experiment, reported in Fig. 1(d).

2.5. Data analysis

All the acquired data from the DCS measurements were analyzed using MATLAB R2022a (The MathWorks Inc., Massachusetts, US). The measured intensity autocorrelation function (g_2) was converted to field autocorrelation function (g_1) using the Siegert relation $g_2(\tau) = 1 + \beta |g_1(\tau)|^2$, where β is a parameter mainly related to the collection optics of the experiment and to the number of speckles in the detection area and τ is the delay time [14]. For the measurements 1-8 in Table 1, and in *in vivo* measurements, this g_1 was fitted with the solution of the correlation diffusion equation for a semi-infinite medium, to retrieve respectively Db and BFI, while only for the measurement 9 in Table 1, where the fibers are immersed in the phantom, fitting was performed with solution of the electric field correlation diffusion equation for an infinite homogeneous medium [14]. To reduce the number of fitting parameters in the fitting procedure, the reduced scattering coefficient μ_s' and the absorption coefficient μ_a were set as fixed values ($\mu_s' = 5\,\mathrm{cm}^{-1}$, $\mu_a = 0.025\,\mathrm{cm}^{-1}$) and β was calculated as the mean of the estimates at the second (400 ns), third (600 ns) and fourth (800 ns) lag times of g_2 curves with a weighted value of 1.5, 1 and 0.5 respectively [36]. In addition, in order to consider diffusing photons, only the first part of the g_1, i.e., $g_1(\tau) > 0.7$ was considered to retrieve Db [37].

For evaluating the precision and reliability of the measurements with different fiber combinations, the standard deviation (σ) of the g_2 at each τ was calculated and plotted along with the averaged g_2 curve ($\bar{g}_2$) from each measurement. To better visualize the variations among the averaged g_2 and g_1 curves from different fiber combinations, their residuals (r) were plotted with respect to the $\bar{g}_2$ and $\bar{g}_1$ curves from Si-Si fiber combination. The ratio of σ(τ) to the $\bar{g}_2(\tau)$ was also calculated and plotted in percentage which is reported as coefficient of variation (CV) [38], together with the theoretical model expectations [39].

Lastly, *in vivo* "fast" blood flow measurements acquired with an acquisition rate of 38 Hz were analyzed to test the capability of the CPG fibers to detect blood flow pulsatile signal [35]. Blood flow signals obtained from both fibers (see Fig. 1(d)) was filtered (low pass Butterworth IIR filter of order 3 with 6 Hz cutting frequency, Matlab function "butter") and normalized, and the Fourier spectral amplitude was calculated separately for every minute of the five-minute acquisition. Signal-to-noise-ratio (SNR) was then calculated, for every minute of acquisition, as the ratio of the Fourier spectral amplitude at the heartbeat frequency, and the background value (i.e. between the first and second harmonic of heart rate frequency [36]. Values reported are the average and standard deviation within the 5-minute acquisition.

3. Results and discussion

3.1. Optical fiber fabrication and characterization

The refractive indices of core and cladding glasses, dimensions (see Fig. 2), *NA* and optical loss of the SM and MM in-house manufactured CPG fibers are reported in Table 2. A homogeneous cross section and a good interface adhesion between core and cladding can be observed in Fig. 2

Biomedical Optics EXPRESS

both for SM and MM fibers, demonstrating the thermo-mechanical compatibility between the core and cladding glasses.

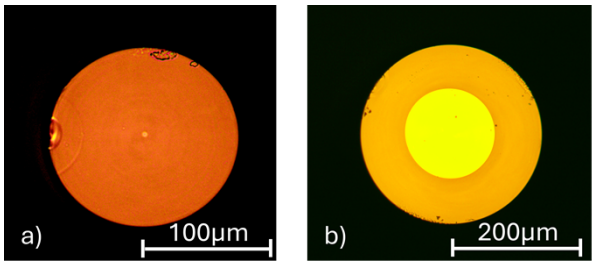

Fig. 2. Optical microscope images of the cross sections of (a) SM and (b) MM fibers realized in-house.

Table 2. Refractive indices of the core and cladding glasses, diameter, numerical aperture and optical losses of the SM and MM fibers fabricated.

Fiber	Core/cladding	Refractive Index (±0.0005)	Diameter(d) (±1 µm)	Numerical Aperture	Optical loss (dB/cm)
SM	Core	1.5293	4.7	0.11	0.60
	Cladding	1.5254	130		
MM	Core	1.5312	220	0.21	0.027
	Cladding	1.5173	400		

To the best of our knowledge, this is the first time that the realization of a SM CPG fiber at 785 nm is being reported. We mention here that, achieving SM CPG fiber near visible wavelength comes with overcoming the associated challenges during the fabrication process. Firstly, CPG is particularly sensitive to compositional variations, which can lead to significant refractive index fluctuations, making it difficult to achieve the necessary small index difference (see Table 2). Similarly, the manufacturing process for CPG of melt quenching (mentioned in section 2.1) is at the limits of precision when trying to achieve a very small refractive index difference. Minor inconsistencies in temperature, mixing, or material purity during glass synthesis can result in a refractive index that deviates from the desired value. Finally, the fiber drawing process requires precise control of temperature, tension, and speed to maintain the desired core and cladding dimensions. CPG is more sensitive to thermal fluctuations compared to silica, and maintaining the required small core size during drawing is at the limits of process control. Any slight variations during drawing can lead to deviations in core size, resulting in fibers that do not maintain SM propagation.

Despite these challenges, the *NA* of the SM and MM CPG fibers was found to be very close to the *NA* values of the commercial silica SM and MM fibers employed in this study (0.13 and 0.22 respectively) for a reliable comparison. The V-number of the SM fiber at 785 nm was then estimated to be 2.05, confirming the SM propagation condition (V-number < 2.405).

The higher loss reported for the SM fiber in Table 2 can be reduced by optimizing the extrusion parameters as explained in [28], yielding a better quality extrudate (cladding tube) in future trials. For compromising this comparatively higher loss reported for SM collection fiber to have sufficient optical signal for DCS measurements, we used shorter (15 cm) sections of CPG SM fiber to collect the scattered photons, connected to the detector via a one-meter SM-commercial silica patch-cord or pigtailed as detailed in section 2.1. The rationale for this choice is based on the possible future applications in long term interstitial monitoring in real clinical scenarios, where meters of implantable optical fiber are not required. Indeed, a short section of the bioresorbable

Biomedical Optics EXPRESS

fiber can be implanted in the region of interest, and the fiber edge protruding outside the body can be terminated with a standard connector and connected to a standard silica patch cord to perform blood flow measurement. This concept has been previously validated in mice [40], using standard commercial MM fibers for long-term optogenetic application.

3.2. *Ex vivo experiments*

In Fig. 3 and Fig. 4, the results of all the *ex vivo* measurements carried out in semi-infinite geometry are reported. Figure 3 corresponds to the measurements performed in configuration-1 while Fig. 4 corresponds to the measurements performed in configuration-2 (see Table 1). The two rows in both the figures corresponds to the measurements with two different source-detector separations, 1.8 and 1.15 cm respectively. Each panel in these figures consists of four curves, representing the simultaneous signal acquisition from two SM detection fibers (one silica and one CPG), where silica and CPG MM fiber are alternatively used to deliver the light, as detailed in section 2.3.

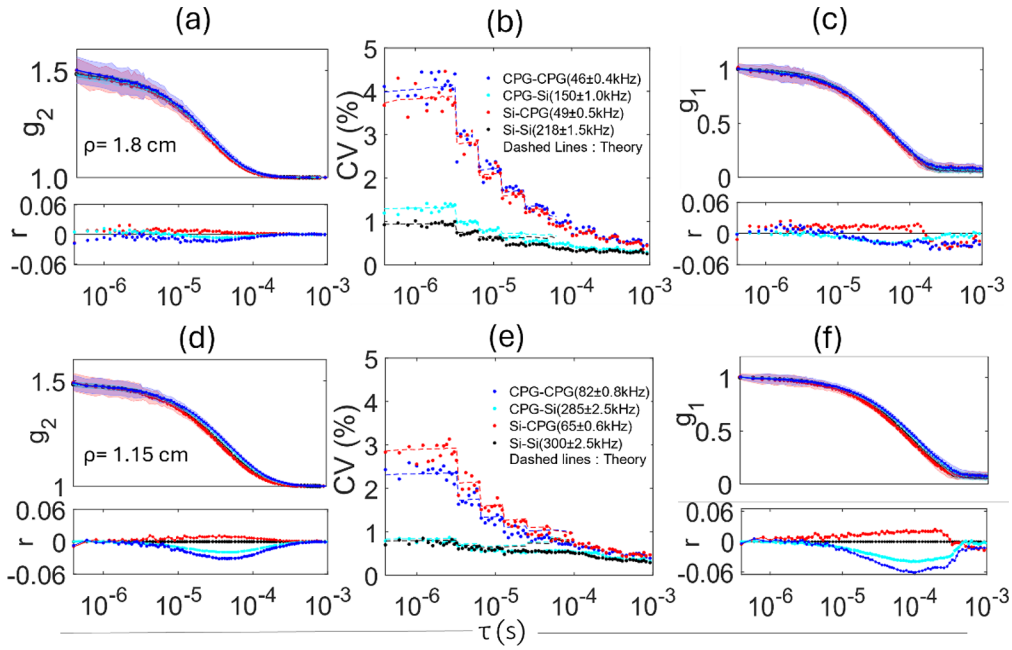

Fig. 3. column 1: g_2 curves averaged over two-minute acquisition (standard deviation is reported as shaded error bars). In (a) curves from measurement 1 and 2 (see Table 1) are reported together with their residual r with respect to the Si-Si fiber combination. In (d) g_2 curves and residuals from measurement 3 and 4 are reported. Column 2: Corresponding coefficient of variation CV of each g_2 curve calculated over two-minute acquisition (in parenthesis the average detected photon count rate) together with theory expectations (dashed lines). Column 3: Corresponding g_1 curves averaged over two-minute acquisition (standard deviation is reported as shaded error bars) with their residual r respect to the Si-Si fiber combination.

In both Fig. 3 and 4, in the first column, the averages of all the 120 g_2 curves (two-minute acquisition) recorded during each measurement are plotted along with their standard deviation as shaded error bars. In the second column, the coefficient of variation CV of the g_2 curves is plotted at each delay time τ together with DCS noise theory expectations [39]. Lastly, in the third column the corresponding average g_1 curves are reported, along with their standard deviation.

Biomedical Optics EXPRESS

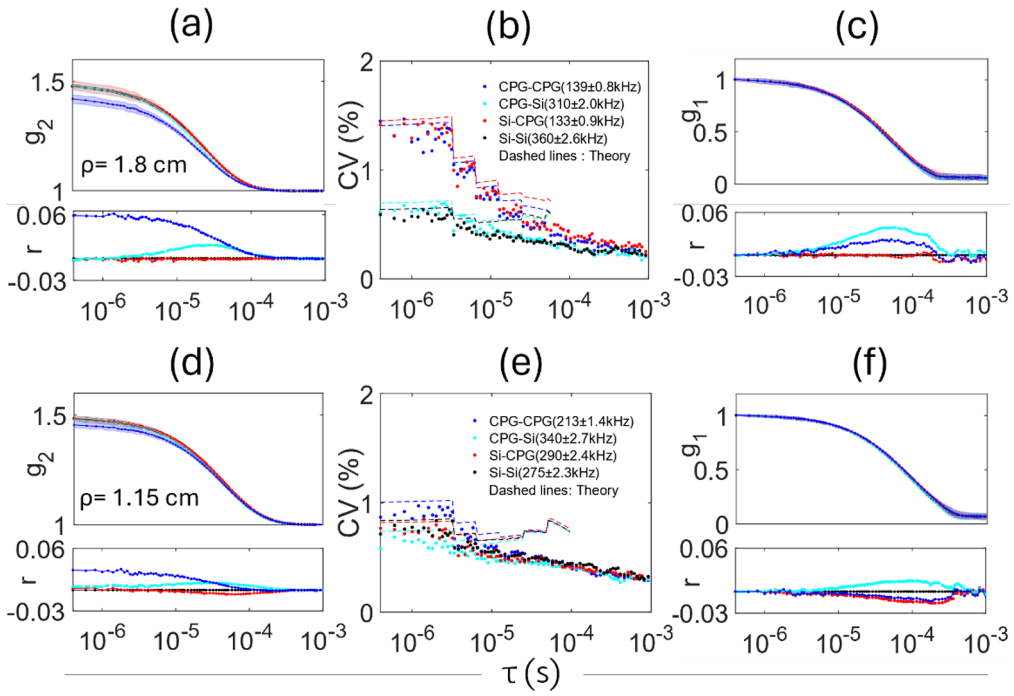

Fig. 4. column 1: g_2 curves averaged over two-minute acquisition (standard deviation is reported as shaded error bars). In (a) curves from measurement 5 and 6 (see Table 1) are reported together with their residual r with respect to the Si-Si fiber combination. In (d) g_2 curves and residuals from measurement 7 and 8 are reported. Column 2: Corresponding coefficient of variation CV of each g_2 curve calculated over two-minute acquisition (in parenthesis the average detected photon count rate) together with theory expectations (dashed lines). Column 3: Corresponding $g_1$curves averaged over two-minute acquisition (standard deviation is reported as shaded error bars) with their residual r respect to the Si-Si fiber combination.

In addition, columns one and three also contain separate panels with plots of residuals r with respect to the $\bar{g}_2$ and $\bar{g}_1$ curves from Si-Si fiber combination.

Plots of g_2 and g_1 show high accordance between the measurements obtained in all the different fiber combinations and configurations (except for the g_2 with CPG source and detector fibers (see Fig. 4(a)), as it will be discussed later on). In all the combinations reported here, g_2 and g_1 residuals with respect to the standard Si-Si case result comparable to g_2 and g_1 error bars (i.e. $< 5\%$). We note that the g_1 curves reported in Fig. 3 and 4 show slightly elevated tails respect to the asymptotic zero value expected from theory for long delay times: this could be due to a possible little contribution in the autocorrelation curves of stray laser light reaching detection fibers while not being diffused by the phantom. Additionally, possible slight β estimation inaccuracies could also contribute.

Plots of the CV qualitatively follows the expectations of the theoretical model of DCS noise [38,39], with a decreasing step function due to the multi-tau arrangement of the correlator. Deviations from the model depend on experimental/environmental conditions and from the fact that the model fails for correlator bin time intervals comparable or larger than the decay time (condition that occurs for larger delay times τ), and for higher count-rates [39,41]. As expected, the precision of the DCS measurement increases as the count rate increases, e.g., ranging from $\sim 3\%$ (at 65 kHz count rate) to $< 1\%$ (at 300 kHz). In all the cases reported, CV is $< 5\%$, an

Biomedical Optics EXPRESS

acceptable precision target for many DCS *in vivo* applications [38]. In addition, plots of the CV show a lower precision (due to the lower detected photon count rate) for the measurements performed with SM CPG detection fibers, highlighting higher optical loss of such fibers. This issue is accentuated in Fig. 3, where the short SM CPG fiber section of 15 cm is connectorized through an FC/PC connector to a standard silica patch cord.

This higher loss is mainly due to the insertion loss in the area of the connector. Slight misalignments between the fiber cores which are of very small size (<5 μm) undergoing the manual connectorization process are possible creating additional optical loss, as previously mentioned in section 2.1, resulting in lower detected photon count rate. We mention that this issue is directly linked to the in-house manufacturing process and can be easily solvable by recurring to professional connectorization.

On the other hand, in the cases where the SM CPG fiber is spliced (Fig. 4), the precision is higher due to the automatic core alignment during hybrid splicing by the CO_2 laser splicer, sensibly reducing optical loss with respect to the manual connectorization process.

In Fig. 5 the β values obtained by averaging all the β from all the 120 acquisitions, are reported together with their standard deviation. The vertical dashed line separates the two detection configurations and the vertical solid lines separate different measurements in each configuration following the numbering of Table 1. Within the error bars, we do not detect any significant difference between all the configurations of fibers (including the infinite medium experiment), except for the CPG-CPG combination in measurement 6 (configuration-2) where the measured β is lower ($\beta = 0.41 \pm 0.013$) possibly due to some light leaks in the fibers. In any case, these detected differences in β do not affect significantly the quality of the g_1 curve utilized for fitting the data, as shown in Fig. 4(f). They indeed show the similar characteristics and decay rates, demonstrating the reliability of measurements irrespective of the fiber combinations used.

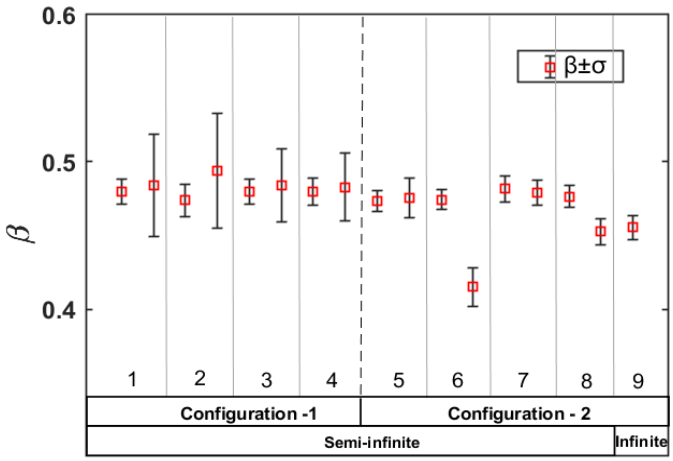

Fig. 5. Estimated β with error bar (standard deviation σ) from all the ex vivo measurements conducted.

Figure 6 shows the retrieved Db from all the *ex vivo* measurements along with their standard deviation. As for Fig. 5, the numbering in the figure corresponds to the measurement order reported in Table 1. Within the two configurations in semi-infinite geometry, considering the error bars, we observe no significant differences in Db obtained from simultaneous measurements. Also, as expected, the estimation is more precise for the measurements with higher photon count rates. Variation in the retrieved Db within and across the different measurement configurations could have stem from the differences in the real and estimated values of input parameters, above all

Biomedical Optics EXPRESS

the source-detector fiber tip separations ρ, and the reduced scattering and absorption coefficients μ_s' and μ_a used in the fitting procedure.

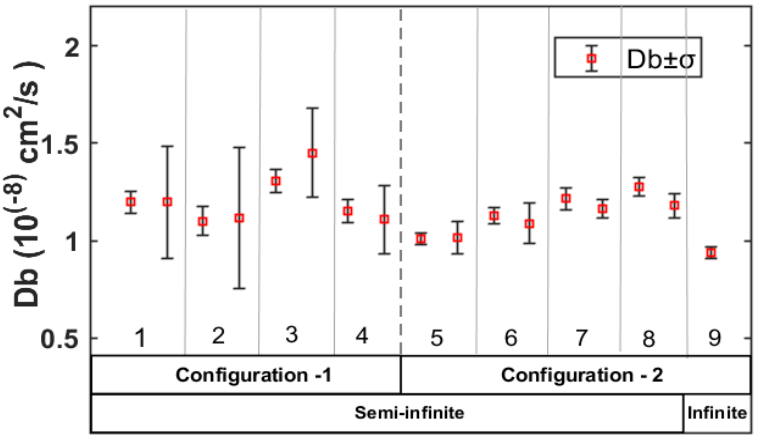

Fig. 6. Estimated Brownian diffusion coefficient with error bar (standard deviation) from all the *ex vivo* measurements conducted.

As the bore size of the standard commercial ceramic ferrules used were larger than the diameter of the custom-made SM and MM CPG fibers (see section 2.3), a complete control of the fiber tip position was not possible during the measurement. This may have caused that the fibers moved slightly inside the ferrules contributing to variations in real ρ value from the estimated value. About the optical properties of the phantom, we mention here that their real values were not quantified but estimated through the recipe reported in [33]. This could have led to differences between estimated and real values, which can amplify differences due to slightly different source detector separations when retrieving Db in the fitting procedure.

Lastly, Fig. 6 also reports the Db related to the experiment performed with the fibers immersed in the liquid phantom (i.e. infinite medium geometry). Even in this case, considering the error bars, we do not detect significant differences between this Db and the ones of all the other fiber configurations tested. Again, the main variations could be due to not perfect control of the fiber positioning (above all depth of the tips) during the experimental procedure and possible phantom degradation (we report here that this measurement was performed on the same phantom but the day after the semi-infinite medium geometry measurements).

3.3. *In vivo experiments*

In Fig. 7, we report the results (blood flow index BFI and detected photon count rates) of the vascular occlusion test performed to validate the capability of the CPG fibers to detect dynamic changes in blood flow.

The figure shows a noisier signal obtained from the CPG detection fiber with respect to the silica one. This is associated with the lower detected photon count rate due to the higher loss of the CPG fiber (for practical experimental purposes, in the *in vivo* experiments, we used the FC/PC connectorized one, that is configuration-1, which shows higher loss). However, in all the phases of baseline, occlusion, and recovery, the BFI curve retrieved using the CPG SM fiber exhibited similar characteristics as of the curve acquired using the standard silica SM fiber. This demonstrates the suitability of CPG fibers to monitor rapid changes of blood flow, with quality comparable to standard commercial fibers.

Exemplary results of "fast" blood flow measurements are reported in Fig. 8(a), where we show an exemplary fifteen second window taken from a five-minute acquisition on the forearm muscle,

Biomedical Optics EXPRESS

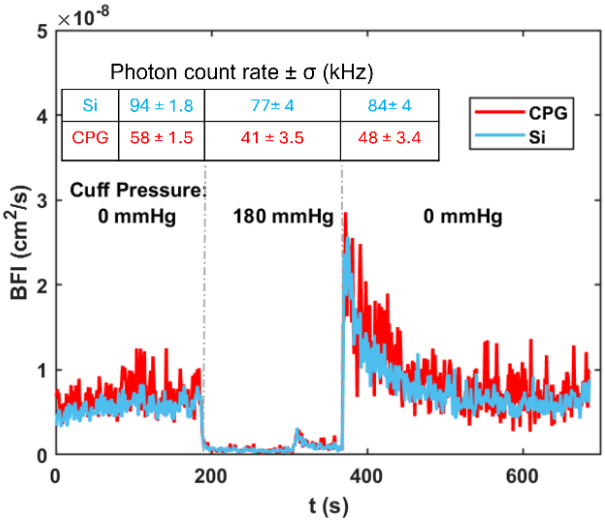

Fig. 7. Estimated blood flow index in cuff-occlusion test, together with the detected photon count rates for the three phases (baseline, occlusion, recovery).

highlighting the blood flow pulsatile signal due to heart beats. The measurement, acquired both with the silica and CPG fibers, reflects a structured signal with peaks and dips that coincide with each other. These peaks and dips correspond to the systolic and diastolic phases of the cardiac cycle. Indeed, Fourier analysis, reported in Fig. 8(b), highlights a principal peak in correspondence of the frequency of approximately 1 Hz, corresponding to the subject heartbeat frequency. As detailed in section 2.4, to compare the capability of the two different fibers used to detect pulsatile signal, we have calculated the signal to noise ratio as the amplitude at the heartbeat frequency divided by the background. The value obtained for the CPG fiber ($SNR_{CPG} = 2.49 \pm 0.15$) results to be only slightly lower than the one obtained for the silica fiber ($SNR_{Si} = 3.16 \pm 0.37$). This is due to the lower detected photon count rate with the CPG fiber (75 kHz ± 4 kHz) than the silica fiber (105kHz ± 6kHz).

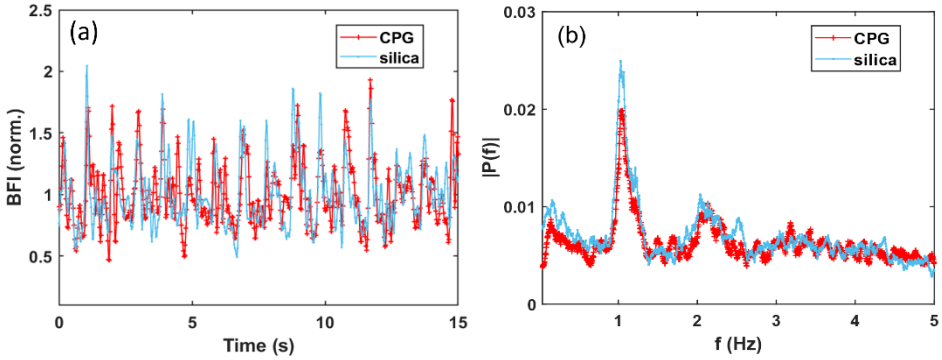

Fig. 8. (a) Exemplary 15s extract of blood flow highlighting fluctuations due to the pulsatile nature of blood flow (b) Fourier Amplitude Spectrum P(f) of BFI waveform obtained considering 5 min acquisition.

We conclude by mentioning that the pulsatile measurements performed both with CPG and silica fibers are not able to resolve the complete cardiac cycle including the dicrotic notch as

Biomedical Optics EXPRESS

reported in [35]. To do this, a better signal to noise ratio is needed (in both cases, silica and CPG), which is commonly obtained by using multi-channel detection systems in combination with single mode fiber bundles [38,42].

4. Conclusions

In this study we reported for the first time the fabrication and the use of single mode and multimode bioresorbable CPG fibers for diffuse correlation spectroscopy. Our measurements demonstrate that the DCS system based on bioresorbable fibers is suitable for recovering the Db of the liquid phantom both in the semi-infinite and infinite medium geometries, with similar quality to the standard commercial fibers. The results from the *in vivo* vascular occlusion test and high-speed pulsatile measurements suggest the suitability of CPG based bioresorbable optical fibers in tracking rapid changes of blood flow along with the potential of capturing the entire cardiac cycle from high temporal resolution data, with a quality comparable to standard silica fibers. These results demonstrate that the use of CPG fibers for diffuse correlation spectroscopy is feasible and represents an interesting perspective for interstitial monitoring of microvascular blood flow using implanted bioresorbable fibers. This can find important implications for example in real time monitoring of therapy effectiveness or following up the evolution after surgical interventions. Combining DCS with different near-infrared spectroscopic techniques for which the bioresorbable fibers have been previously validated [12,13], within a single resorbable photonic platform in future can bring immense potential in retrieving continuous complementary physiological information which can be collectively used for planning, optimizing and in predicting or monitoring the outcomes for example in interstitial photodynamic therapy [43].

The future work will focus on continuous long-term (over a period of few weeks) *ex vivo* measurements to assess the signal stability over time with the degradation of the fiber. Finally, the preliminary results obtained from the *ex vivo* and non-invasive *in vivo* measurements reported here are promising in terms of designing and performing future in *vivo* validation experiments using CPG fibers in animal models for interstitial hemodynamic monitoring.

Funding. European Union's HORIZON EUROPE Marie Sklodowska-Curie Actions (860185); Fundación Cellex; Fundació Mir-Puig; Agencia Estatal de Investigación (PID2023-151973OB-I00 PHOTOSHOCK, PID2023-147553OB-I00 SCOSWear, PLEC2022-009290 SAFEICP); "Severo Ochoa" Programme for Centres of Excellence in R&D (CEX2019-000910-S); MEDLUX/LUXMED special program; Generalitat de Catalunya (AGAUR-2022-SGR-01457, CERCA, RIS3CAT-001-P-001682 CECH); European Union's Horizon 2020 Framework Programme (VASCOVID 101016087, Prometeus 101099093, fastMOT 101099291); FEDER EC and Laserlab-Europe; National Institutes of Health; ISCIII (DTS, FIS).

Acknowledgments. This work was carried out under the PHAST project that has received funding from the European Union's Horizon 2020 research and innovation programme under grant agreement No. 860185. The authors also acknowledge Fundació CELLEX Barcelona, Fundació Mir-Puig, Agencia Estatal de Investigación (PID2023-151973OB-I00 PHOTOSHOCK, PID2023-147553OB-I00 SCOSWear, PLEC2022-009290 SAFEICP), the "Severo Ochoa" Programme for Centres of Excellence in R&D (CEX2019-000910-S), MEDLUX/LUXMED special program, Generalitat de Catalunya (CERCA, AGAUR-2022-SGR-01457, RIS3CAT-001-P-001682 CECH), the European Union's Horizon 2020 research and innovation programme (VASCOVID 101016087, Prometeus 101099093, fastMOT 101099291), FEDER EC and LASERLAB-EUROPE, NIH, ISCIII (DTS, FIS) for partially funding the study.

Disclosures. Turgut Durduran is an inventor on relevant patents (US8082015B2, EP18382664.3A). ICFO has equity ownership in the spin-off company HemoPhotonics S.L. Potential financial conflicts of interest and objectivity of research have been monitored by ICFO's Knowledge & Technology Transfer Department. No financial conflicts of interest were identified. The authors declare no additional conflicts of interest.

Data availability. Data underlying the results presented in this paper are not publicly available at this time but may be obtained from the authors upon reasonable request.

References

1. A. A. La Mattina, S. Mariani, and G. Barillaro, "Bioresorbable materials on the rise: from electronic components and physical sensors to in vivo monitoring systems," Adv. Sci. **7**(4), 1902872 (2020).

Biomedical Optics EXPRESS

2. J. Shin, Z. Liu, W. Bai, *et al.*, "Bioresorbable optical sensor systems for monitoring of intracranial pressure and temperature," Sci. Adv. **5**(7), eaaw1899 (2019).
3. W. Bai, J. Shin, R. Fu, *et al.*, "Bioresorbable photonic devices for the spectroscopic characterization of physiological status and neural activity," Nat. Biomed. Eng. **3**(8), 644–654 (2019).
4. W. Bai, H. Yang, Y. Ma, *et al.*, "Flexible transient optical waveguides and surface-wave biosensors constructed from monocrystalline silicon," Adv. Mater. **30**(32), 1801584 (2018).
5. C. M. Boutry, H. Chandrahalim, P. Streit, *et al.*, "Towards biodegradable wireless implants," Philos. Trans. R. Soc., A **370**(1967), 2418–2432 (2012).
6. G. Keiser, F. Xiong, Y. Cui, *et al.*, "Review of diverse optical fibers used in biomedical research and clinical practice," J. Biomed. Opt. **19**(8), 080902 (2014).
7. M. Rezapour Sarabi, N. Jiang, E. Ozturk, *et al.*, "Biomedical optical fibers," Lab. Chip **21**(4), 627–640 (2021).
8. J. C. Knowles, "Phosphate based glasses for biomedical applications," J. Mater. Chem. **13**(10), 2395–2401 (2003).
9. J. T. Pandayil, N. G. Boetti, and D. Janner, "Advancements in biomedical applications of calcium phosphate glass and glass-based devices-a review," J. Funct. Biomater. **15**(3), 79 (2024).
10. E. Ceci-Ginistrelli, D. Pugliese, N. G. Boetti, *et al.*, "Novel biocompatible and resorbable UV-transparent phosphate glass based optical fiber," Opt. Mater. Express **6**(6), 2040 (2016).
11. O. Podrazký, P. Peterka, I. Kašík, *et al.*, "In vivo testing of a bioresorbable phosphate-based optical fiber," J. Biophotonics **12**(7), e201800397 (2019).
12. L. Di Sieno, N. G. Boetti, A. Dalla Moras, *et al.*, "Towards the use of bioresorbable fibers in time-domain diffuse optics," J. Biophotonics **11**(1), e201600275 (2018).
13. V. Damagatla, N. G. Boetti, L. D. Sieno, *et al.*, "Use of bioresorbable fibers for interstitial time-domain diffuse optical spectroscopy with fast gating," in *Diffuse Optical Spectroscopy and Imaging IX* (Optica Publishing Group, 2023), paper 1262818.
14. T. Durduran, R. Choe, W. B. Baker, *et al.*, "Diffuse optics for tissue monitoring and tomography," Rep. Prog. Phys. **73**(7), 076701 (2010).
15. D. A. Boas, L. E. Campbell, and A. G. Yodh, "Scattering and imaging with diffusing temporal field correlations," Phys. Rev. Lett. **75**(9), 1855–1858 (1995).
16. D. A. Boas and A. G. Yodh, "Spatially varying dynamical properties of turbid media probed with diffusing temporal light correlation," J. Opt. Soc. Am. A **14**(1), 192–215 (1997).
17. D. A. Boas, S. Sakadžić, J. J. Selb, *et al.*, "Establishing the diffuse correlation spectroscopy signal relationship with blood flow," NPh **3**(3), 031412 (2016).
18. G. Yu, "Near-infrared diffuse correlation spectroscopy in cancer diagnosis and therapy monitoring," J. Biomed. Opt. **17**(1), 010901 (2012).
19. E. M. Buckley, A. B. Parthasarathy, P. E. Grant, *et al.*, "Diffuse correlation spectroscopy for measurement of cerebral blood flow: future prospects," Neurophotonics **1**(1), 011009 (2014).
20. T. Durduran and A. G. Yodh, "Diffuse correlation spectroscopy for non-invasive, micro-vascular cerebral blood flow measurement," Neuroimage **85**(Part 1), 51–63 (2014).
21. S. A. Carp, M. B. Robinson, and M. A. Franceschini, "Diffuse correlation spectroscopy: current status and future outlook," Neurophotonics **10**(01), 013509 (2023).
22. Q. Wang, M. Pan, L. Kreiss, *et al.*, "A comprehensive overview of diffuse correlation spectroscopy: theoretical framework, recent advances in hardware, analysis, and applications," NeuroImage **298**, 120793 (2024).
23. T. M. Busch, "Local physiological changes during photodynamic therapy," Lasers Surg. Med. **38**(5), 494–499 (2006).
24. G. Yu, T. Durduran, C. Zhou, *et al.*, "Real-time in situ monitoring of human prostate photodynamic therapy with diffuse light," Photochem. Photobiol. **82**(5), 1279–1284 (2006).
25. D. R. Busch, W. Lin, C. C. Goh, *et al.*, "Towards rapid intraoperative axial localization of spinal cord ischemia with epidural diffuse correlation monitoring," PLoS One **16**(5), e0251271 (2021).
26. F. A. Jenkins and H. E. White, *Fundamentals of Optics* (McGraw-Hill, 2018).
27. B. E. A. Saleh and M. C. Teich, *Fundamentals of Photonics* (John Wiley & Sons, 2019).
28. D. Gallichi-Nottiani, D. Pugliese, N. G. Boetti, *et al.*, "Toward the fabrication of extruded microstructured bioresorbable phosphate glass optical fibers," Int. J. Appl. Glass Sci. **11**(4), 632–640 (2020).
29. E. Ceci-Ginistrelli, C. Smith, D. Pugliese, *et al.*, "Nd-doped phosphate glass cane laser: from materials fabrication to power scaling tests," J. Alloys Compd. **722**, 599–605 (2017).
30. R. Hui and M. O'Sullivan, *Fiber-Optic Measurement Techniques* (Academic Press, 2022).
31. "Thorlabs - FN96A Guide to Connectorization and Polishing of Optical Fibers," https://www.thorlabs.com.
32. L. Cortese, G. Lo Presti, M. Zanoletti, *et al.*, "The LUCA device: a multi-modal platform combining diffuse optics and ultrasound imaging for thyroid cancer screening," Biomed. Opt. Express **12**(6), 3392–3409 (2021).
33. L. Cortese, G. Lo Presti, M. Pagliazzi, *et al.*, "Liquid phantoms for near-infrared and diffuse correlation spectroscopies with tunable optical and dynamic properties," Biomed. Opt. Express **9**(5), 2068–2080 (2018).
34. K. D. Didier, S. M. Hammer, A. M. Alexander, *et al.*, "Microvascular blood flow during vascular occlusion tests assessed by diffuse correlation spectroscopy," Experimental Physiol. **105**(1), 201–210 (2020).
35. D. Wang, A. B. Parthasarathy, W. B. Baker, *et al.*, "Fast blood flow monitoring in deep tissues with real-time software correlators," Biomed. Opt. Express **7**(3), 776–797 (2016).

Biomedical Optics EXPRESS

36. J. Fischer, "Transcranial diffuse optical measurements of pulsatility derived parameters for neuromonitoring applications", PhD Thesis, ICFO-The Institute of Photonic Sciences/ Universitat Politècnica de Catalunya 2021.
37. J. Selb, D. A. Boas, S.-T. Chan, *et al.*, "Sensitivity of near-infrared spectroscopy and diffuse correlation spectroscopy to brain hemodynamics: simulations and experimental findings during hypercapnia," Neurophotonics **1**(1), 015005 (2014).
38. L. Cortese, G. Lo Presti, M. Pagliazzi, *et al.*, "Recipes for diffuse correlation spectroscopy instrument design using commonly utilized hardware based on targets for signal-to-noise ratio and precision," Biomed. Opt. Express **12**(6), 3265–3281 (2021).
39. C. Zhou, G. Yu, D. Furuya, *et al.*, "Diffuse optical correlation tomography of cerebral blood flow during cortical spreading depression in rat brain," Opt. Express **14**(3), 1125–1144 (2006).
40. D. R. Sparta, A. M. Stamatakis, J. L. Phillips, *et al.*, "Construction of implantable optical fibers for long-term optogenetic manipulation of neural circuits," Nat. Protoc. **7**(1), 12–23 (2012).
41. D. Biganzoli and F. Ferri, "Statistical analysis of dynamic light scattering data: revisiting and beyond the Schätzel formulas," Opt. Express **26**(22), 29375–29392 (2018).
42. G. Dietsche, M. Ninck, C. Ortolf, *et al.*, "Fiber-based multispeckle detection for time-resolved diffusing-wave spectroscopy: characterization and application to blood flow detection in deep tissue," Appl. Opt. **46**(35), 8506–8514 (2007).
43. C. P. Lowdell, D. V. Ash, I. Driver, *et al.*, "Interstitial photodynamic therapy: clinical experience with diffusing fibres in the treatment of cutaneous and subcutaneous tumours," Br. J. Cancer **67**(6), 1398–1403 (1993).